# Selective Delamination upon Femtosecond Laser Ablation of Ceramic Surfaces

Frederik Kiel,[1,*] Nadezhda M. Bulgakova,[2] Andreas Ostendorf,[1] and Evgeny L. Gurevich[1]

[1]*Applied Laser Technologies, Ruhr-Universität Bochum, Universitätsstraße 150, 44801 Bochum, Germany*
[2]*HiLASE Centre, Institute of Physics of the Czech Academy of Sciences, Za Radnicí 828, 25241 Dolní Břežany, Czech Republic*

We report on the experimental observation of selective delamination of semitransparent materials on the example of yttria-stabilized zirconia ceramics upon femtosecond laser processing of its surface with a low numerical aperture lens. The delamination of a ceramic layer of dozens of micrometers takes place as a side effect of surface processing and is observed above the surface ablation threshold. The onset of delamination (delamination threshold) depends on the degree of overlap of the irradiation spots from consecutive laser pulses upon beam scanning over material surface. Analysis of the delaminated layer indicates that the material undergoes melting on both of its surfaces. The mechanism of delamination is identified as a complex interplay between the optical response of laser-generated free-electron plasma and nonlinear effects upon laser beam propagation in semitransparent ceramics. The discovered effect enables controllable laser microslicing of brittle ceramic materials.

## I. INTRODUCTION

Ultrashort-pulse laser micromachining of materials is attracting growing interest due to the possibility of achieving much higher quality of the laser-processed surfaces as compared to longer laser pulses [1]. The enhanced processing quality is largely conditioned by the difference in the laser ablation mechanisms for ultrashort (at the range from femtoseconds to dozens of picoseconds) laser pulses as compared to longer pulses. The difference results from strong thermal and stress confinements inherent for ultrashort laser pulses [2]. Although generally the conditions of stress confinement can be achieved at different pulse durations [2], at ultrashort laser pulses this effect is more distinct, so that the ablation can occur in the form of mechanical fracture and ejection of a layer of the irradiated material (referred to as spallation) as a result of the development of tensile stresses [3,4].

Spallation of laser-irradiated materials from the front target surface and from the rear surface in the case of films/foils has been extensively studied both experimentally [5–12] and theoretically [3,4,7,13]. In all experiments on the rear surface spallation of metals, the irradiation spot size was considerably larger than the metal film thickness [5–7,9]. It has been proven that the rear-side spallation effect is conditioned by the reflection of the laser-induced shock wave from the rear surface with the formation of a region with a high strain rate sufficient for the creation

of voids/cracks. For the case of front surface spallation, which can also manifest itself as swelling, the spalled layers were found to be of a submicrometer thickness with the size dependent on the materials' properties [10–12].

In this paper, we report on front-side delamination of a layer from yttria-stabilized zirconia (YSZ) foil upon femtosecond laser processing of its surface with a low numerical aperture lens. Here, we call this effect "delamination" to underline the difference from the spallation mechanism mentioned above. In our case, delamination takes place from the front side of the target irradiated with multiple laser pulses at fluences $F$ exceeding the surface ablation threshold. The delaminated layer thickness is from ten to several dozens of micrometers. This thickness depends on the irradiation conditions. It must be underlined that the irradiation spot size on the material surface is much smaller as compared to the thickness of the YSZ samples. We discuss the physical mechanisms of this effect and demonstrate that delamination happens due to a complex interplay of the two major phenomena, self-focusing of the laser beam transmitted toward the material bulk and its defocusing by the free-electron plasma generated in the surface layer of the sample.

It is noteworthy that recently Kim *et al*. [14] have reported on using femtosecond laser pulses for slicing 4H-SiC wafers by tight beam focusing (NA = 0.8) to a desired depth inside the sample. By using this method, exfoliation of an approximately 260-$\mu$m 4H-SiC layer was achieved with smaller roughness and material losses as compared to conventional slicing techniques. The laser

---

*kiel@lat.rub.de

irradiation conditions used in the present study differ considerably from those of Ref. [14]: the beam was focused on the sample surface with a low numerical aperture lens. However, because of the highly nonlinear properties of YSZ ceramic, the observed delamination effect that is analyzed below can have some analogy with that reported in Ref. [14].

## II. EXPERIMENTAL SETUP

Our experiments are performed with the diode-pumped fiber laser Tangerine produced by Amplitude Systems, emitting in TEM$_{00}$ mode at a wavelength of 1030 nm and a pulse duration of 290 fs [full width at half maximum (FWHM)]. The repetition rate is scalable up to 2 MHz. The laser beam quality factor $M^2$ is about 1.15 and the beam diameter $D_{\text{FWHM}}$ is about 1.25 mm at the laser output. The downstream beam expander by Thorlabs expands the beam diameter by a factor of 3 to 3.75 mm. The beam is directed by a set of mirrors to the Galvo-scanner SCANcube 7 by SCANLAB. At the scanner output, an $F$-theta lens with a focal length of $f = 63$ mm (numerical aperture 0.06) by SCANLAB focuses the beam on the sample surface located on the XYZ stage with the $z$ axis parallel to the laser beam. Processed areas are either $0.5 \times 0.5$ mm$^2$ or $5 \times 5$ mm$^2$. The beam waist in the focal plane is $w_0 \approx 7.5$ $\mu$m and the Rayleigh-length $z_R \approx 149$ $\mu$m is close to the thickness of the irradiated sample.

The yttria-stabilized zirconia (or 8YSZ) used in these studies is zirconium dioxide with 8% of yttrium oxide molar percentage, which is added to stabilize the cubic lattice. We notice, however, that recent publications indicate that a complete stabilization at room temperature is not achieved and there are inclusions of the tetragonal phase, the so-called t" [15]. The melting point of 8YSZ is about 2700°C. Further material data are given in Table I. The samples are provided by Forschungszentrum Jülich GmbH, IEK1 purchased from KERAFOL. Dimensions of the samples are $25 \times 25 \times 0.2$ mm$^3$.

## III. RESULTS AND DISCUSSION

### A. General features of 8YSZ processing

Depending on the processing parameters (laser fluence and overlap of the irradiation spots upon scanning) different modes of sample modification/ablation are observed. We define the ablation threshold as the highest fluence at which no visible modification is seen in white-light interferometry (WLI). Additionally, we introduce a threshold fluence for the onset of delamination, $F_{\text{th}}^{\text{delam}}$. This threshold is determined as the lowest investigated fluence at which a layer of delaminated material can be found on the top of the laser-processed area, though this layer can cover the processed area only partially. These two thresholds are slightly varying from one to another set of the experiments that can be conditioned by the initial sample defects. They depend on the scanning speed and the pulse repetition rate. As shown below, varying the scanning speed can compensate, to a certain extent, for the change in the repetition rate to ensure a similar overlap (OL). However, the delamination threshold and the delaminated layer thicknesses can be slightly different for the same overlaps at different repetition rates that can be referred to as the heat accumulation effect. Below, we give the thresholds as the ranges of fluence in which either ablation or delamination (ablation or delamination threshold, respectively) start to be observed in all of our experiments.

Figure 1 demonstrates typical scanning electron microscope (SEM) images of laser-processed surfaces when delamination is either not observed or partially seen. Between the two above-defined thresholds, the processed area does not contain microparticulates and is relatively smooth as demonstrated in Fig. 1(a). At fluences just above the delamination threshold for a particular overlap, the delaminated layer covers the processed surface only partially as shown in Figs. 1(b) and 1(c). It is always attached to the side of the processed area where laser scanning is started. That can be an indication of an accumulation effect, which leads to destroying the delaminated layer upon continued scanning. The roughness of the unprocessed

TABLE I. Physical properties of 8YSZ.

| Characteristics | Formula symbol | Value | Unit |
| --- | --- | --- | --- |
| Crystal lattice [16] | ... | cubic | ... |
| Band gap [17] | $E_g$ | 5.3 | eV |
| Density[a] | $\rho$ | 5950 | kg m$^{-3}$ |
| Absorbtion depth at 1030 nm[b] | $l_a$ | 53 | $\mu$m |
| Reflection coefficient at 1030 nm[b] | $R$ | 0.52 | |
| Heat capacity [18] (20°C) | $c_p$ | 500 | J kg$^{-1}$ K$^{-1}$ |
| Heat capacity [18] (1200°C) | $c_p$ | 670 | J kg$^{-1}$ K$^{-1}$ |
| Thermal conductivity [18] | $\lambda_{\text{th}}$ | 2.2 | W m$^{-1}$ K$^{-1}$ |
| Thermal diffusivity (20°C) | $\kappa$ | $7.4 \times 10^{-7}$ | m$^2$ s$^{-1}$ |

[a]Manufacturer specification.
[b]Obtained for virgin samples by measuring transmission and reflectance using UV-3600plus by SHIMADZU.

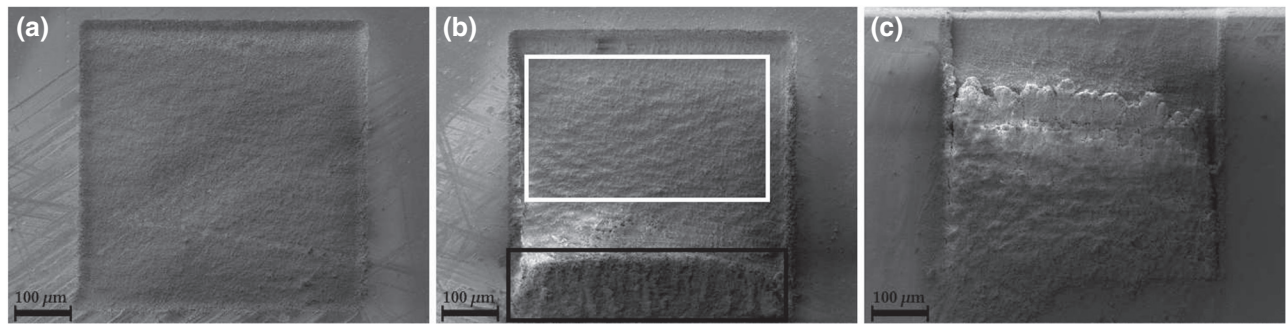FIG. 1.    SEM images of the laser-processed areas. (a) OL = 22% and $F = 20.1$ J cm$^{-2}$. No delamination features are observed. (b) OL = 75% and $F = 24.9$ J cm$^{-2}$. The greater part is clean of any particulates (outlined by the white frame), while the delaminated layer can be seen in the black-framed region. (c) OL = 83% and $F = 8.8$ J cm$^{-2}$. The delaminated layer covers a substantial part of the processed surface (bottom part of the image) and its boundary in the form of flakes is clearly seen at the top part of the image.

YSZ surfaces is 0.15 $\mu$m. The roughness of the processed areas in Figs. 1(a) and 1(b) (in the white-framed area) is 0.5 $\mu$m and 2 $\mu$m, respectively.

With further increasing fluence or overlap, the area becomes fully covered by the delaminated layer and the thickness of the layer increases as clearly seen in Fig. 2(a) (areas marked by the numbers 20, 19, and 18). The figure presents the cross-sectional image of the processed area with the delaminated layers. To obtain this image, the sample is cut across the processed areas. It should be noted that, in these cases of delamination, all three surfaces are modified with clear signs of melting, on both the top and bottom of the delaminated layer, as well as the surface from which delamination occurred. Also, it can be noticed that

the delaminated layer rises up somewhat from the initial sample surface. Figure 2(b) presents the magnified view of the contact between the delaminated layer and the underlying sample, as well as the edge where the processed and virgin sample areas are in contact. The SEM image in Fig. 2(c) shows a freestanding delaminated layer obtained due to a particular breakout at the cutting edge. The perspective is 30° tilted from the upright position. Fig. 2(d) shows that the bottom surface of this delaminated layer is modified.

Here, we hypothesize that, below the delamination threshold, the observed ablation of ceramics also proceeds via delamination but the delaminated layer is too thin. As a result, it is destroyed, most probably mechanically, via
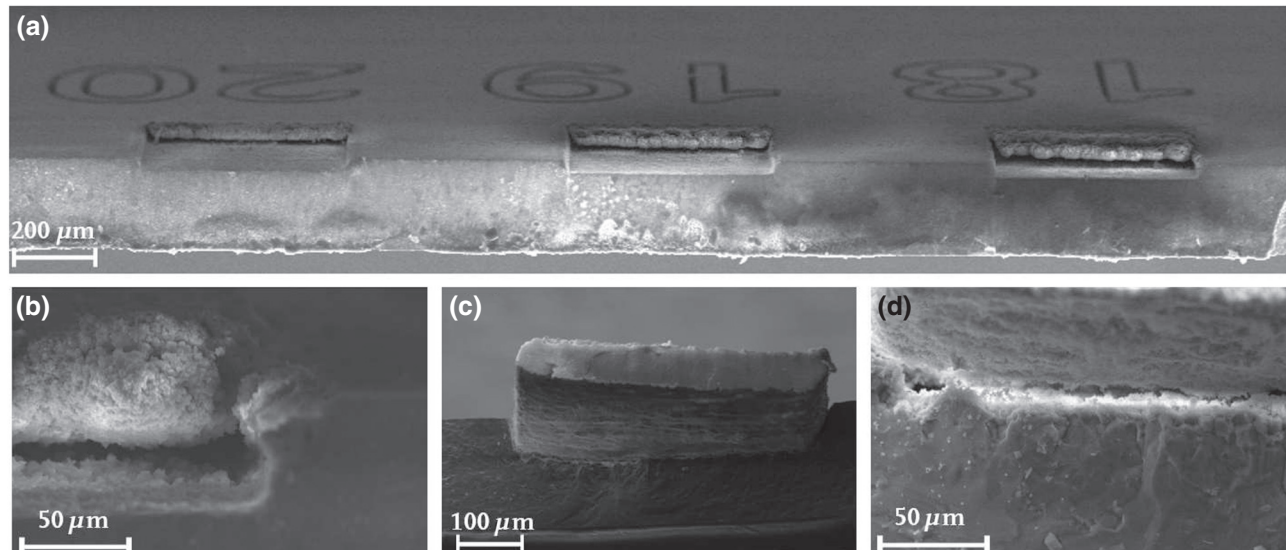


FIG. 2.    SEM images of laser-processed areas with different fluences. Overlap (83.1%) and repetition rate (100 kHz) are constant for all cases shown. (a) Cross-sectional view of the laser-processed sample (30°-tilted view). The laser fluences are 7.2, 7.9, and 8.6 J cm$^{-2}$ (marked as 20, 19, and 18, respectively). (b) Magnified view of the edge of the processed area (a) 18 in contact with the virgin sample area. Melting and ablation features can be recognized. (c) The 30°-tilted view of the delaminated layer at a laser fluence of 17.2 J cm$^{-2}$. (d) Magnified view of (c), showing the contact between the delaminated layer and the underlying sample.
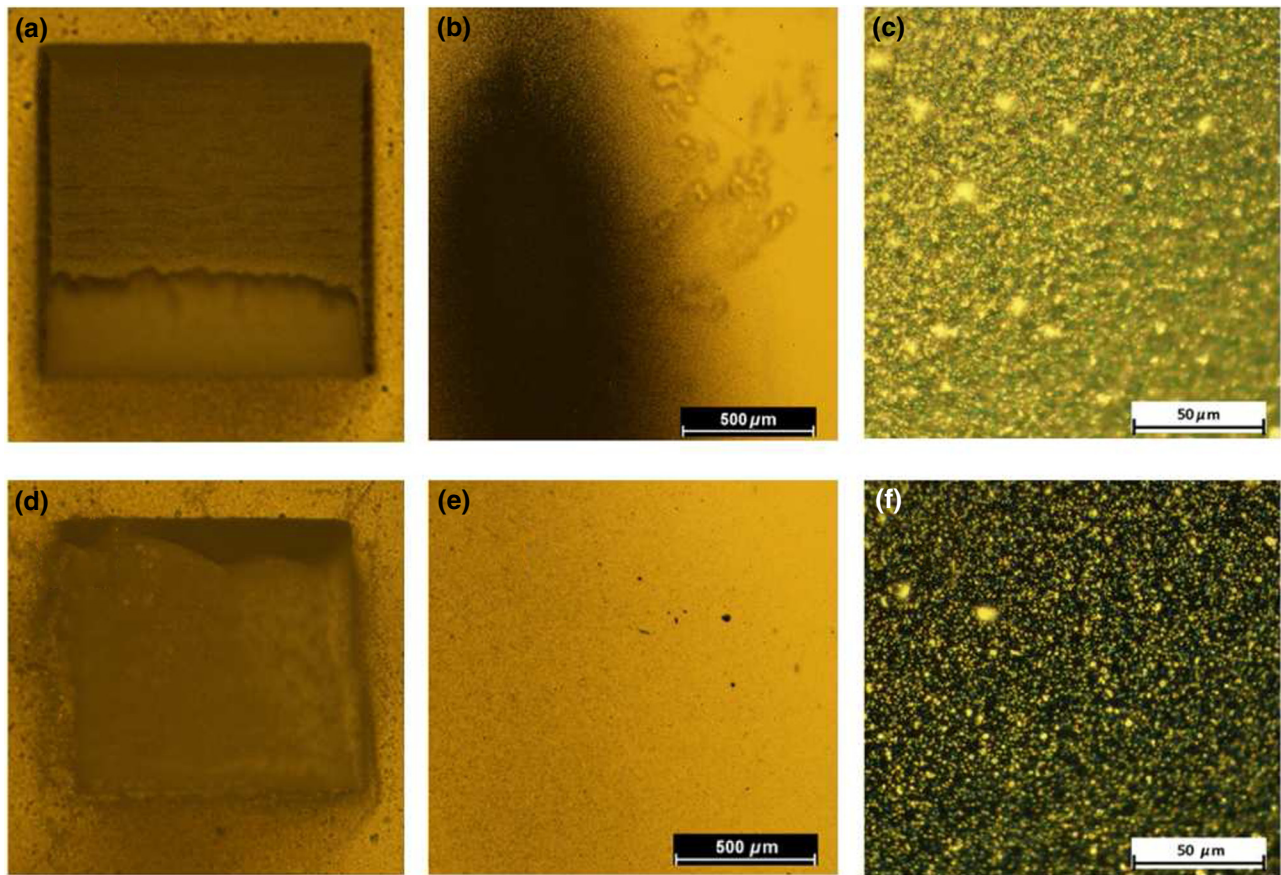
FIG. 3. (a)–(c) Images of the laser-processed area at a fluence of $1.6 \, \text{J cm}^{-2}$ obtained by optical microscopy. (a) partly destroyed delaminated layer, (b) corresponding glass substrates with the deposit of the ablation products in bright field and (c) in dark field. The delaminated layer is partially destroyed and its large fragments are clearly seen on the substrates. (d)–(f) The same for a laser fluence of $5.7 \, \text{J cm}^{-2}$ when the whole delaminated layer remains attached to the sample. Only small rare particulates can be recognized on the substrate. $\text{OL} = 92\%$ for all images.

cracking and ejection from the processed sample. With increasing thickness, the delamination layer withstands cracking and remains attached to the sample. This assumption can be verified by the inspection of the deposit of the ablation products on a collecting substrate. To do this, a microscope glass substrate is placed slightly to the side of the laser beam, still assuring the laser plume deposition. The results are shown in Fig. 3 for the irradiation spot overlap of 92%. The upper row presents images of the processed area (a) and glass substrate in bright (b) and dark (c) fields for a laser fluence of $1.6 \, \text{J cm}^{-2}$. The delaminated layer is partially destroyed and, consequently, its large fragments are abundantly deposited on the substrates. At the same time, at a laser fluence of $5.7 \, \text{J cm}^{-2}$ when the delaminated layer remains completely attached to the sample (d), only small rare particulates can be recognized on the glass substrate.

Below, we address this assumption in more detail and provide the most probable physical mechanism of the observed delamination phenomenon.

## B. Ablation depth and delaminated layer thickness

Based on the above assumption that the visible ablation naturally transfers to delamination with increasing laser fluence (note that the delaminated layer remaining on the sample after processing can be mechanically removed from the processed area), we introduce here a unified ablation depth as the difference between the levels of virgin surface and the bottom of either the ablated (without delamination signs) or delaminated area. The unified ablation depth is determined by white-light interferometry, using the Polytec TMS 1200 with Mirau objectives. According to the device specification, the uncertainty in the step measurement varies between 0.18 and 0.1 $\mu$m depending on the step size. The reproducibility of the method is tested by measuring 15 different areas made on different YSZ samples with the same processing parameters. The standard deviation of the measurements is approximately 0.8 $\mu$m, which reveals a certain deviation in the studied YSZ samples. For areas that are not fully covered by the delaminated layer, it is measured in the

TABLE II. Fluence and peak power ranges, starting from which delamination is observed. The data are presented for several overlaps and the two repetition rates, 200 and 100 kHz. The corresponding unified ablation depths as well as pulse-to-pulse and line-to-line shifts, $\Delta x$ and $\Delta y$, respectively, are also given.

| Overlap (%) | $\Delta x$ ($\mu$m) | $\Delta y$ ($\mu$m) | $F_{th}^{delam}$ (J cm$^{-2}$) | Peak power (MW) | Unified ablation depth ($\mu$m) | Repetition rate (kHz) |
|---|---|---|---|---|---|---|
| 92 | 1 | 1 | 2.2–2.6 | 13–15 | 11.2 | 200 |
| 83 | 2 | 2 | 4.3–4.9 | 26–30 | 15.7 | 200 |
| 75 | 3 | 3 | 9.6–10.4 | 59–63 | 18.4 | 200 |
| 75 | 3 | 3 | 12.7–13.5 | 78–82 | 22.8 | 100 |
| 67 | 4 | 4 | 22.9–23.9 | 140–146 | 23.1 | 100 |

regions free of delamination features. For the processed areas completely covered by the delamination layer, the corresponding cross-sectional images are analyzed.

Table II outlines the tendencies of the unified ablation depth evolution as a function of overlap between irradiation spots. The ablation depths are given at the delamination thresholds indicated as the fluence ranges (see comment above) for two repetition rates, 100 and 200 kHz. The overlaps in the $x$ and $y$ directions are always the same as indicated in the table by sample shifts $\Delta x$ and $\Delta y$ between two subsequent pulses along the scanning line and between subsequent scanning lines, respectively. All processed areas here are the same, $0.5 \times 0.5$ mm$^2$. Decreasing overlap requires a higher fluence to observe the delaminated layer. Similarly, when decreasing the repetition rate while preserving the overlap, higher fluences have to be applied to obtain the delaminated layer attached to the processed surface. We note here that $F_{th}^{delam}$ is typically several times higher than the ablation threshold. Thus, for 75% overlap and 200 kHz, the ablation threshold is found to be in the range of 2.2–2.6 J cm$^{-2}$, four times smaller than $F_{th}^{delam}$ at this regime of processing; see Table II.

Figure 4 presents the unified ablation depth (see the definition above) as a function of (a) fluence and (b) energy density dose $\Theta$, which is defined as the product

of single-pulse energy and the total number of pulses per area divided by the processed area size. All the results presented are obtained with two repetition rates of 100 and 200 kHz and three overlaps between pulses and lines, 67%, 75%, and 83%. The symbols outlined in Fig. 4(a) as circles refer to the processing regimes above the delamination thresholds. Based on Fig. 4, several features of the ablation/delamination process can be highlighted:

(a) The depth increases monotonically for increasing fluence [Fig. 4(a)] and increasing energy density dose [Fig. 4(b)]. There are no visible peculiarities that would indicate a transition from "pure" ablation to delamination.

(b) Increasing overlap at a constant single-pulse fluence considerably increases the unified ablation depth.

(c) Twice increasing the repetition rate has a tendency to slightly increase the unified ablation depth.

(d) The energy density dose defines the unified ablation depths as clearly seen from Fig. 4(b).

(e) A similar unified ablation depth can be achieved by different parameter sets of overlap and fluence that correspond to the same energy density dose. As shown in Sec. III D, the fraction of the delaminated layer, which remains attached to the processed sample, depends on the overlap and the number of scans.
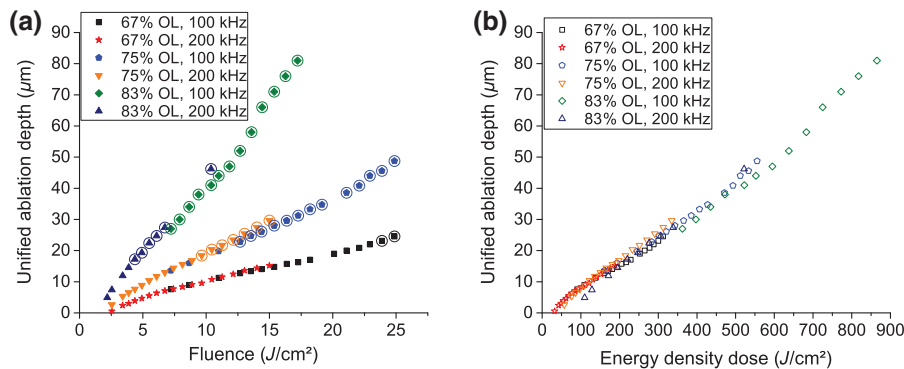


FIG. 4. (a) Unified ablation depth as a function of laser-pulse fluence for different overlaps and repetition rates. Circled data points correspond to fluences for which a delaminated layer could be observed. (b) Unified ablation depth as a function of the energy density dose. No significant difference in the ablation depth can be observed for similar energy doses when varying the parameter set of OL and fluence.

(f) Interestingly, in all cases, the delaminated layer survives on the processed area when the ablation reaches approximately 20 $\mu$m (somewhat smaller for higher overlap and slightly larger for smaller overlap).

The last feature indicates that the delaminated layer thinner than approximately 20 $\mu$m experiences cracking, fractures, and is ejected from the processed surface as proven in Fig. 3, where large fragments of ceramics deposited on a collecting substrate are demonstrated for the processing regimes below $F_{th}^{delam}$. Upon reaching a certain depth, the layer becomes able to withstand against cracking and remains attached to the sample. As a whole, the outlined features count in favor of delamination/fracturing of an essentially mechanical nature whose mechanism is addressed in Sec. III E.

### C. Structure of the delaminated layer

Figure 5 presents the typical SEM images of the top surface of the delaminated layer and of the sample beneath it. It is apparent that ablation/modification of material occurs both on the top of the delaminated layer and at its contact with the remaining sample. The inset shows an unirradiated area with the grain sizes significantly larger than the particles seen on the irradiated surfaces. Remarkable is that the signs of the initial grained structure can be recognized in the ablation relief; see Fig. 5(a). The reason is a high concentration of defects in grain boundaries that provokes a preferred ablation at the boundary sites [19]. Hence, this image supports considerable ablation from the external surface of the delamination layer that must be mediated by the laser-induced breakdown and free-electron plasma formation at the sample surface [20].

X-ray diffraction (XRD) measurements are carried out with the X`Pert Pro by PANalytical, used in Bragg-Brentano geometry. XRD characterizations of unprocessed and processed areas, the latter in the regimes with and without delamination, show no differences, indicating that the processed surfaces, including the delaminated layer, have the same polycrystalline structure as the unprocessed material.

### D. Repetition rate and heat accumulation

As already indicated in Table II and Fig. 4, a lower repetition rate results in a higher $F_{th}^{delam}$. This result can also be seen in Fig. 6. For all four processed areas in the middle grayscale image, pulse fluence (11 J cm$^{-2}$) and overlap (83%) are the same and only repetition rate is changed in this series of laser processing from the upper left image to the lower right one from 100 to 50, 25, and 10 kHz, respectively. The ablation depths for these processed areas are 40.3, 38.3, 35.9, and 34.8 $\mu$m, respectively. The noticeable decrease in the ablation depth with decreasing repetition rate can be attributed to the heat accumulation effect. The heat accumulation at the surface layer of the sample should lead to the thermal expansion of the layer and correspondingly to a somewhat lower refractive index in the heat-affected zone. This process should consequently result in some defocusing of the laser-beam part penetrating toward the sample bulk. According to the mechanism of delamination proposed below in Sec. III E, beam refocusing deep in the sample produces the delamination cut. The surface layer expanding due to the heat accumulation effect can shift the cut deeper to the bulk at the higher repetition rates. Although heat accumulation can also cause thermal lensing, the absorbed heat is mostly confined in the delaminated layer and its gradient across the beam radius can be insufficient to counterbalance the thermal expansion effect. We suppose here that the ejection of the material due to a self-focusing cut in its depth does not occur at each laser pulse but happens periodically as a result of stress accumulation from several pulses; see Sec. III E.

The delaminated layer is clearly seen as a lighter region within the processed square-shaped area in the images. It is almost completely preserved on the sample without destruction at the highest repetition rate of $f = 100$ kHz,
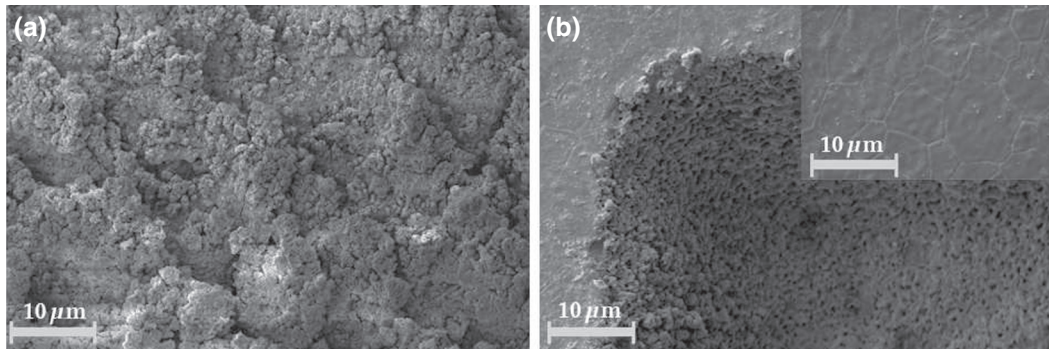


FIG. 5.   (a) Typical view of the ablation features on the top of the delaminated layer. (b) Morphology of the sample surface beneath the delaminated layer. The inset shows an unirradiated sample surface with observable grain boundaries. Images are obtained by scanning electron microscopy. The overlap between the irradiation spots is 75%; laser fluence is 17.2 J cm$^{-2}$.
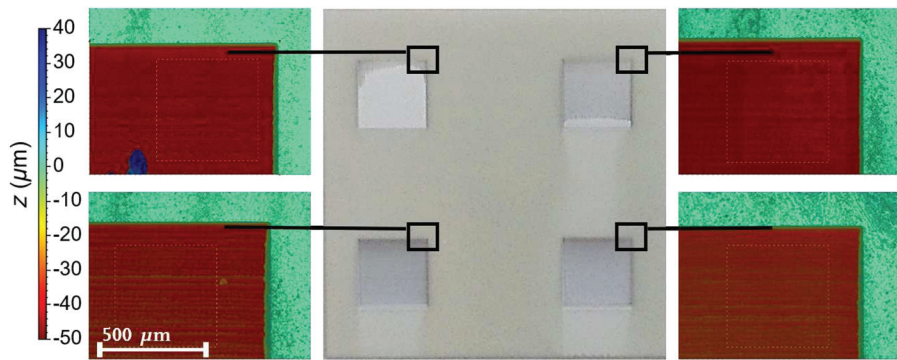
FIG. 6. $5 \times 5$-mm$^2$ processed areas irradiated with $F = 11 \, \mathrm{J \, cm^{-2}}$ (photograph in the middle). The repetition rates are 100 kHz (in the upper left panel, the maximum depth of processing, $H$, is 40.3 m); 50 kHz (upper right, $H = 38.3$ m); 25 kHz (lower left, $H = 35.9$ m); and 10 kHz (lower right, $H = 34.8$ m). The decrease in the repetition rate is compensated by the scanning velocity to keep the same overlap of 83%. The delaminated layers appear as lighter regions within the process areas. Note that processing is performed horizontally with gradual shifting of the scanning lines from the bottom to the top in each processed area. Magnified views represent the WLI images. The scale and color map are applicable to all four WLI images.

while for lower repetition rates the remaining delaminated layer considerably decreases in size (Fig. 6). It is worth mentioning that the light shadows beneath the bottom parts of the processed areas for 50, 25, and 10 kHz originate from the redeposition of particulates from the ablation plume, while, at 100 kHz, when the delaminated layer is almost completely preserved on the processed area, no visible signs of particulate redeposition are observed. The most plausible explanation is seen again in the heat accumulation effect emerging at higher repetition rates. Indeed, it is known that ceramics usually become less brittle at enhanced temperatures [21]. Hence, the higher the repetition rate, the higher the temperature in the delaminated layer and the longer this layer can withstand fracturing upon laser scanning. Note that the delamination of the irradiated layer from the sample confines the absorbed energy within the layer, thus enhancing the heat accumulation effect.

The important role of heat accumulation has also been confirmed in the following series of experiments. In this series, the number of pulses per each processed area of $0.5 \times 0.5$ mm$^2$ and the single pulse fluence (and hence, the energy density dose) are kept constant. For the first two processed areas, all pulses are applied in one scanning run with high overlaps between the irradiation spots, 83% (0.97-s scanning time) and 75% (0.52-s scanning time), which correspond to 62 500 and 27 777 pulses per area, respectively. Two other areas are processed in four scanning runs but with smaller overlaps of the irradiation spots within each scan (67%, 0.33-s time per scan and 51%, 0.18-s time per scan). As a result, the total numbers of pulses per area are the same as for the first two areas, 62 500 and 27 777, respectively. However, in the case of fourfold scanning with smaller OL, the energy density dose is four times smaller in each scan as compared to a single scan with high overlap. Additionally, to lower the heating

in each scan, the heat accumulated during one scan has time to partially dissipate by the time of the next scan. As a result, fourfold scanning provides colder conditions of material processing.

Figure 7 shows the WLI images of the processed areas of $0.5 \times 0.5$ mm$^2$ with 62 500 pulses. The applied single pulse fluence is $15.4 \, \mathrm{J \, cm^{-2}}$ and the energy density dose is $760 \, \mathrm{J \, cm^{-2}}$ for the processed area, resulting in the ablation depth of approximately 61.4 $\mu$m in both single and fourfold scanning. However, in the single run, almost the whole delaminated layer survives on the sample and only a very small region in the upper part of the processed area is evidently destroyed and ejected from the sample as seen in Fig. 7(a) (note that laser processing is started at the bottom edge of the image). On the contrary, at fourfold scanning with smaller overlap and time delays between subsequent scanning runs that should ensure better heat dissipation, only a small part of the delaminated layer survives on the sample [Fig. 7(b)]. These experiments demonstrate that heat accumulation plays an important role in preventing destruction of the delaminated layer.

Figure 8 shows the WLI images of the processed areas of $0.5 \times 0.5$ mm$^2$ with 27 777 pulses at a laser fluence of one pulse of $20.1 \, \mathrm{J \, cm^{-2}}$, resulting in an energy density dose $\Theta = 440 \, \mathrm{J \, cm^{-2}}$ for the processed area. On the surface processed by a single scanning run with an overlap of 75%, the delaminated layer is partially preserved, being attached to the edge from which scanning is started [Fig. 8(a)]. The ablation depth is 36.1 $\mu$m in this case. In the area processed four times with 51% overlap, the ablation depth is somewhat smaller than at 75% overlap, 34.6 $\mu$m [but comparable in regard to the standard deviation of 0.8 $\mu$m of measurements (see Sec. III B)], while no signs of the delamination layer are visible [Fig. 8(b)]. Also, it can be noticed that the delamination layer is rising up from the sample surface by about 40 $\mu$m. It looks like
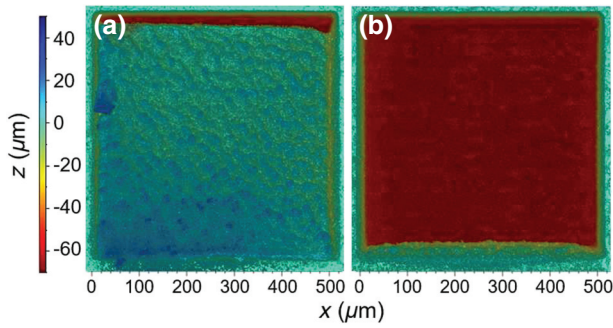
FIG. 7. The areas of $0.5 \times 0.5$ mm$^2$ processed with the same number of pulses, 62 500. (a) Overlap of 83%, single scanning run. (b) Overlap of 67%, four scanning runs. In both cases, the applied fluence is $F = 15.4$ J cm$^{-2}$, and the energy density dose $\Theta = 760$ J cm$^{-2}$. Laser processing is started from the bottom edge of the image with scanning lines along the $x$ direction. Images are obtained by WLI.



FIG. 8. Same as in Fig. 7 for 27 777 pulses per $0.5 \times 0.5$ mm$^2$ area. (a) Overlap of 75%, single scanning run. (b) Overlap of 51%, four scanning runs. The applied fluence is $F = 20.1$ J cm$^{-2}$, and the energy density dose $\Theta = 440$ J cm$^{-2}$. Laser processing is started from the bottom edge of the image with scanning lines along the $x$ direction. Images are obtained by WLI.

a flake, being attached to the sample at the starting edge of processing and lifted off at the rest area, that is plausible due to pushing forces upon the delamination cut/crack formation [Fig. 8(a)].

Figures 7 and 8 clearly indicate the dominating role of the energy density dose in regard to the ablation depth and the heat accumulation effect in regard to the delaminated layer stability. Although the laser fluence is higher for a smaller number of pulses applied to the same area, the ablation depth and, hence, the delamination layer thickness are considerably smaller. To explain this and other features of the delamination effect, below we consider the processes taking place upon laser beam coupling to band-gap materials and discuss possible mechanisms and scenarios of the delamination effect.

### E. Possible mechanism of observed delamination: Counterbalancing between self-focusing and electron plasma antiwaveguiding

Ceramic delamination can be explained by laser beam self-focusing upon propagation in the nonlinear optical medium. In nonlinear media, the refractive index $n$ depends not only on the frequency of the electromagnetic field but also on the local field intensity of the laser beam $I(r, z, t)$ as $n = n_0 + n_2 I(r, z, t)$, where $n_0$ and $n_2$ are the linear and nonlinear (Kerr) refractive indexes and $r$ and $z$ are, respectively, radial and axial coordinates. For transparent crystals and glasses, the value of $n_2$ is typically positive and in the range of $10^{-16}$ to $10^{-14}$ cm$^2$ W$^{-1}$ [22]. The wave front of powerful laser beams with the intensity increasing toward the axis (e.g., Gaussian as in our case) is distorted during beam propagation in such a nonlinear medium, as schematically shown in Fig. 9(a), due to decreasing phase velocity in higher refractive index regions [23]. As a result, initially parallel optical rays are converging toward the
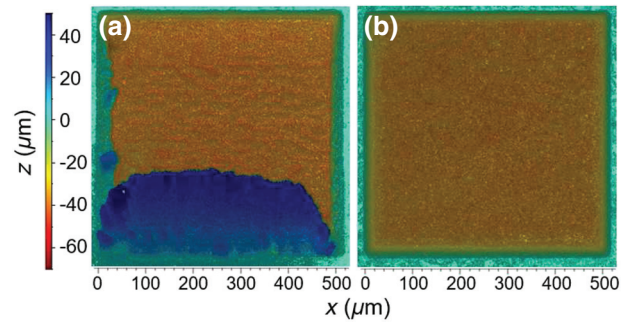
beam axis, culminating in catastrophic collapse at a distance $z_{SF1}$ after the laser beam enters into the medium. The critical laser power for self-focusing, which is derived from the balance between the angles of self-focusing $\theta_{SF}$ and beam diffraction $\theta_{df}$, $\theta_{SF} = \theta_{df}$, can be evaluated as $P_{cr} \approx 3.72 \lambda_0^2 / (8 \pi n_0 n_2)$, where $\lambda_0$ is the laser wavelength [24,25].

For yttria-stabilized zirconia at a laser wavelength of 1030 nm, $n_0 = 2.1236$ and $n_2 = 1.184 \times 10^{-15}$ cm$^2$ W$^{-1}$. Using these data, the critical power for self-focusing can be evaluated as approximately 0.63 MW, which is more than an order of magnitude smaller than the smallest threshold value of beam power for delamination; see Table II. For transparent (low-absorbing) media, the propagation depth of the beam till its collapse can be estimated by the empirical expression [24,25]

$$L_c = \frac{0.367 z_R}{\sqrt{[(P_{in}/P_{cr})^{0.5} - 0.852]^2 - 0.0219}}. \quad (1)$$

Here, $P_{in}$ is the power of the incident laser beam. We suppose that in our experiments the layer is delaminated at the depth of self-focusing $L_c$. Assuming as the first approximation that material absorption is insignificant before the beam collapses, one can evaluate $L_c \approx 11$ $\mu$m at a fluence of 2.5 J cm$^{-2}$. Interestingly, this pair of values coincides with the threshold of delamination at high overlap [92% (see Table II)]. We can presume that, at such low laser fluences, only a small fraction of light is absorbed before beam collapsing and, hence, the depth of beam collapse is reasonably described by Eq. (1). Indeed, for the intrinsic (linear) absorption depth of 53 $\mu$m of YSZ ceramics (assuming the absence of nonlinear absorption), less than 20% of the beam energy is absorbed at the distance of 11 $\mu$m and the Kerr focus is shifted insignificantly.

However, as follows from Eq. (1), the self-focusing distance has to move closer to the sample surface with
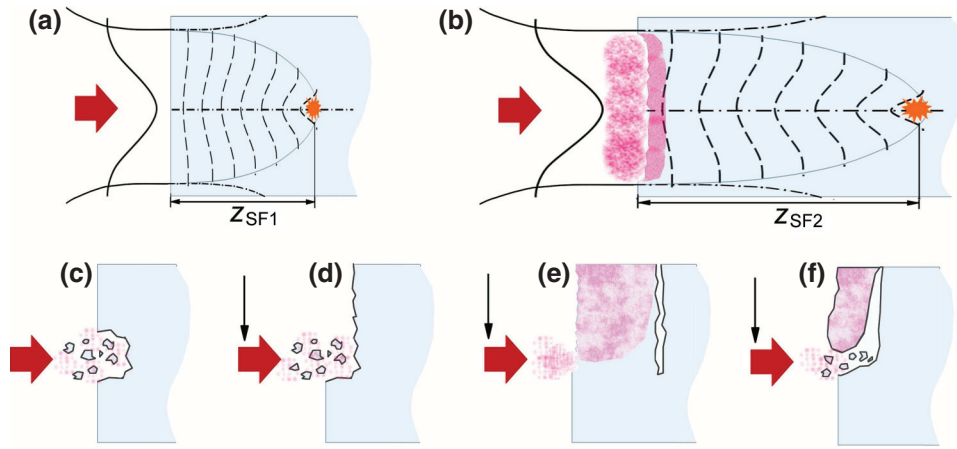
FIG. 9. (a) Illustration of laser beam self-focusing in a transparent nonlinear solid with a high ionization threshold. The beam is focused on the sample surface. Instead of diverging after the geometrical focus (dashed-dotted lines), the beam experiences self-focusing governed by the Kerr effect until its collapse at the distance $z_{SF1}$, which culminates with the generation of free-electron plasma. The scheme has been adapted from Ref. [23]. (b) For semitransparent materials like ceramics considered in this paper, free-electron plasma is already generated at the surface layer (pink surface region) that can lead to melting and ablation of the surface layer. The free-electron population counteracts the Kerr effect by adding a negative contribution to the refractive index; see Eq. (2). This "antiwaveguiding" effect [23] is stronger for higher energy of the beam. As a result, self-focusing is delayed in space and the self-focusing distance $z_{SF2}$ is increasing with laser beam power. (c)–(f) Schematics of the ablation/delamination mechanism. At relatively low laser power (but above the self-focusing threshold), the beam collapse happens close to the surface [as in (a)], resulting in fracturing the region between the collapse spot and the surface (c). In such regimes with scanning (the scanning direction is shown by the black arrow), mechanical fracturing with ejection of ceramic fragments is the main mechanism of ablation (d). At high laser power, generation of a dense electron plasma in a thin surface layer leads to partial reflecting of laser light and in the antiwaveguiding effect [23]. As a result, the laser beam fraction, which is transmitted through the electron plasma layer, collapses deep in the target and provides the material melting, ablation, and fracturing inside the bulk that is seen during the layer delamination (e). At intermediate beam powers, the layer delamination can transform to layer fracturing upon scanning (f) as seen in Figs. 6, 7, and 8.

increasing beam power. Thus, for the fluence of $7\,\mathrm{J\,cm^{-2}}$, $L_c \approx 7.4\ \mu$m, which is more than 3 times smaller as compared to the unified ablation depth for the overlap of 83% (Fig. 4, 200-kHz repetition rate). Below we show that there is no contradiction as, for semi-transparent materials irradiated with loose beam focusing on the surface and at high repetition rates, other effects can contribute to the position of the self-focus.

The transient and permanent changes of the refractive index in laser-irradiated materials can be caused by several factors, which include the Kerr effect ($\Delta n_{\mathrm{Kerr}}$), generation of conduction-band electrons ($\Delta n_{\mathrm{CB}}$), heat accumulation ($\Delta n_{\mathrm{th}}$), accumulation of defects ($\Delta n_{\mathrm{def}}$), density change in the heat-affected zone ($\Delta n_{\rho}$), and local stress ($\Delta n_P$) [26–28]:

$$\Delta n = \Delta n_{\mathrm{Kerr}} + \Delta n_{\mathrm{CB}} + \Delta n_{\mathrm{th}} + \Delta n_{\mathrm{def}} + \Delta n_{\rho} + \Delta n_P. \tag{2}$$

The contribution of the Kerr effect is positive, resulting in narrowing and, finally, collapsing the laser beam [Fig. 9(a)]. Upon beam collapsing, a high local intensity is achieved, which is enough to create free electrons. A free-electron population is produced via photo-ionization, which can trigger collisional ionization starting from a

certain level of free electrons [20]:

$$\frac{dN_e}{dt} = (\sigma_k I^k + \alpha_{\mathrm{col}} N_e I)\frac{(N_0 - N_e)}{N_0}. \tag{3}$$

Here, $N_e$ is the density of free electrons, $N_0$ is the atomic density of unexcited material, $\sigma_k$ and $k$ are the coefficient and the order of multiphoton ionization respectively, and $\alpha_{\mathrm{col}}$ is the coefficient of collisional ionization. The factor $(N_0 - N_e)/N_0$ is added to account for the available ionization centers at high ionization rates [29]. It should be underlined that, at ultrashort laser pulses, the avalanche ionization can considerably contribute to the generation of free electrons in band-gap materials. Thus, Lenzner *et al.* [30] have shown that, in fused silica, the avalanche process is developing already at laser pulses of 120-fs duration, which leads to a strong decrease in the processing quality compared to shorter laser pulses. Furthermore, numerical simulations [31] have demonstrated that, for fused silica at 300-fs laser pulses, the avalanche process contributes noticeably to material ionization already starting from approximately $2 \times 10^{13}$ W/cm$^2$ and Eq. (3) is applicable at intensities $\gtrsim 4 \times 10^{13}$ W/cm$^2$ (see Fig. 3 in Ref. [31]). Note that such intensities are typical for our experiments, while the smaller band gap of YSZ ceramics ($E_g = 5.3$ eV against 9 eV for fused silica) should

result even at lower intensities in free carrier generation, subsequently triggering the avalanche process.

As soon as free-electron plasma is produced in the conduction band, it counteracts the Kerr self-focusing ($\Delta n_{CB} < 0$) and can even lead to the antiwaveguiding effect [23]. In our case, when the laser beam is loosely focused on the sample surface with generation of free electrons in the surface layer according to Eq. (3), the free-electron plasma can considerably alter the beam coupling to the material via increasing reflectivity, light defocusing/scattering, and attenuating the beam along its propagation toward the material bulk after a partial reflection from the electron plasma at the surface layer. Within a surface layer where the laser beam is not yet strongly distorted by self-focusing and defocusing, attenuation of laser intensity can be roughly described in a one-dimensional form as

$$\frac{dI}{dz} = -\alpha_{in}I - \sigma_k I^k \frac{(N_0 - N_e)}{N_0}k\hbar\omega - \alpha_{fe}I. \quad (4)$$

Here, $\alpha_{in} = 1/l_a$ is the intrinsic absorption coefficient and $\alpha_{fe}$ is the absorption coefficient of free electrons produced by the laser light. The optical response of the dynamically ionized dielectric target (both dynamic change of the reflection coefficient and the spatiotemporal behavior of $\alpha_{fe}$) can be calculated through the complex dielectric function $\epsilon(N_e)$ by involving the Drude theory [29].

A dynamically evolving reflectivity of the beam from the sample surface and attenuation of its part penetrating toward the sample bulk have to strongly affect the position of the Kerr focus under the condition that the beam power remains in excess of $P_{cr}$ after the beam passes through the excited surface region. It can be stated that the Kerr focus is dynamic under such excitation conditions and its position depends on the fraction of the beam energy (power) that has passed through the free-electron-plasma "shield" generated in the surface layer. Generally, the transient plasma "mirror/attenuator" created in the surface layer of the sample should move the Kerr focus deeper to the material bulk as schematically shown in Fig. 9(b). We recall that, at 7 J cm$^{-2}$, $P_{in}/P_{cr} \approx 68$, yielding $L_c \approx 7.4$ $\mu$m as estimated by Eq. (1). It is possible to roughly evaluate that, to move the Kerr focus deeper into the sample, to approximately 27 $\mu$m from the surface (Fig. 4), the beam power must decrease by a factor of approximately 8.3 after partial reflection and attenuation by the free-electron plasma at the surface layer (to achieve $P/P_{cr} \approx 8.1$–$8.2$ after passing the plasma layer). Note that, in such a case, the laser fluence drops from 7 J cm$^{-2}$ at the sample surface to a local level below 1 J cm$^{-2}$; the latter is much smaller than the damage threshold of a wide band-gap dielectric (the estimated direct band gap of yttria-stabilized zirconia is around 5.2–5.8 eV [32]). Here, damage means any irreversible change of material that is observed after laser irradiation, such as visible signs of

melting, material ablation, cracking, change of crystalline structure, compaction, or appearance of porosity. Note that the minimal laser fluence starting from which the damage is observed (damage threshold) is scaling with the band gap of dielectric materials and for materials with $E_g > 5$ eV it exceeds 1 J cm$^{-2}$ at pulse durations of 100 fs and longer [33]. Upon self-focusing, the intensity of the attenuated laser beam can reach again the value sufficient for the free-electron production, which in turn induces local material heating and stress generation, in analogy with Ref. [14], where the laser beam was purposely focused inside a 4H-SiC wafer with a high numerical aperture lens. Hence, the laser-induced free electron plasma created upon focusing the laser beam on the sample surface can reasonably explain the delamination effect and its depth found in this work.

Reliable numerical simulations of the experimental conditions presented here are not seen as possible in light of the extremely large computational resources required for such kinds of problems (see, e.g., Ref. [34]) and a number of unknown material parameters for the description of free-electron generation. To estimate light reflection and absorption by the generated free-electron plasma, we recall that, even for the materials with a larger band gap such as fused silica under similar surface-irradiation conditions, an overcritical free-electron density is produced within the laser fluence range used in the present experiments [35]. According to simulations for fused silica (see Fig. 6 in Ref. [35]) and taking into account the intrinsic reflectivity of 8YSZ ceramics (Table I), at a laser fluence of approximately 7 J cm$^{-2}$ (a peak fluence of approximately 14 J cm$^{-2}$), more than half of the laser energy is reflected from the surface. The rest of the laser energy, which penetrates into the sample, is attenuated due to photoionization and absorption by free electrons during propagation toward the target. The attenuated energy density can exceed 3 J cm$^{-2}$ at a distance of approximately 4 $\mu$m. Note that, for this estimation, we assume that an average energy spent for free-electron production and heating is in the range of 50–60 eV per electron, which is consistent with simulations [35] and experiments [36]. Under such conditions of laser energy absorption, the laser beam is attenuated to the fluence below the damage threshold, but still it has a power above $P_{cr}$ with respect to the self-focusing effect. Note that, additionally, the laser beam can be scattered (defocused) by the free-electron plasma. In view of a lower band gap of yttria-stabilized zirconia as compared to fused silica, the generated free-electron density can be even higher than considered in the above estimations and results in a higher light absorption within the surface layer. Hence, the scenario presented in Fig. 9(b) seems to be plausible and convincing:

(a) With increasing beam energy, the laser-generated electron plasma in the surface layer of the sample strongly

depletes the laser beam. The absorbed laser energy in this layer is enough to induce melting and even partial ablation at the sample surface.

(b) The fraction of the beam, which passes through the free-electron region, is not sufficiently energetic to cause material damage.

(c) However, as the power of the beam is still above $P_{cr}$, the beam experiences self-focusing with the Kerr focus much deeper into the sample as compared to what could be expected for the case of absent or weak absorption. As a result, a new local region of high laser energy absorption appears in the Kerr focus, inducing new damage (melting, cracking, and internal ablation).

Regarding the ablation/delamination mechanisms, the following conclusions can be drawn based on the above considerations. At relatively low laser fluences (but above the self-focusing threshold in terms of pulse power), the free-electron density generated in the surface layer of the sample as well as the linear material absorption are insufficient to induce the surface damage. As a result, after partial reflection from the surface and absorption in the surface layer, the beam penetrates toward the bulk and collapses in the subsurface region. In the collapse region, because of the formation of a highly localized free-electron population that transfers its energy to the lattice upon recombination at the time scale of a few picoseconds, ceramics must melt and a very high stress is generated. It has been shown that, in the beam-focusing region deep inside a fused silica bulk, the stress level is of the order of 70–80 MPa [34]. In YSZ ceramics under similar focusing conditions, the maximum stress level is expected to be more than an order of magnitude higher. Indeed, the stress is proportional to the Young's modulus (approximately 2.5–3 times higher for YSZ [37] as compared to fused silica) and the coefficient of thermal expansion (approximately $10^{-5}$ $K^{-1}$ for YSZ [38] against $0.55 \times 10^{-6}$ $K^{-1}$ for fused silica) [39]. As the tensile strength of YSZ ceramics is reported to be 745 MPa [40], the expected stress has to considerably exceed the material strength, leading to mechanical damage around the collapse region. As estimated above, at relatively low beam powers and, hence, in the absence of or at low free-electron plasma shielding, the self-focus has to be formed close to the sample surface. The laser-induced stress, which exceeds the material strength, should cause fracturing of the material layer between the focus and the surface with ejection of particulates [Fig. 9(c)]. In such regimes, mechanical fracturing of the surface layer is the main mechanism of ablation upon laser processing [see Fig. 9(d)], which has been confirmed by experiments with the deposition of the ablation products (Fig. 3). The smallest fluence at which such material removal starts to be observed is considered the ablation threshold. Noticeable is that the ablation thresholds for different processing conditions (pulse repetition rates,

irradiation spot overlap) differ insignificantly [Fig. 4(a)]. It is known that, at ultrashort laser irradiation of bandgap materials, the surface damage threshold drops dramatically with the number of pulses applied to the same surface area due to material-dependent incubation effects [41]. An insignificant difference in the ablation thresholds at different overlaps upon laser scanning observed in our experiments supports the idea that the ablation process is governed by beam self-focusing, which is weakly dependent on incubation effects in the surface layer of the sample. Nevertheless, it can be expected that, upon laser scanning, not every pulse leads to material fracturing but ejection of particulates happens periodically as a result of stress accumulation from several laser pulses.

At high beam powers, a high-density free-electron plasma is formed at the very surface layer of the sample, which results in shielding and antiwaveguiding of the laser beam. The fraction of the beam that penetrates through the shielding area experiences collapse at a large distance from the surface, as discussed above. In such cases, the stress generated in the self-focus region is not enough to induce fracturing of a relatively thick material layer between the self-focus and the surface. The high-temperature/high-pressure local zone inside the bulk evolves into a pore [34]. Namely, in such regimes, the delamination effect over the whole processed area is developing, which originates from the line of the adjacent or closely located pores [Fig. 9(e)]. At intermediate laser powers, the delaminated layer can be preserved on the sample up to a certain level of accumulated stress, after which it is starts to fracture during further processing [Fig. 9(f)]. The area of the preserved delaminated layer depends on the depth of self-focusing and the overlapping degree; the latter determines the heat accumulation in the delaminated layer and, hence, its mechanical properties.

It is necessary to admit that, because of the multiplicity of factors influencing light propagation in materials [Eq. (2)], the delamination effect uncovered in this work is a very complex phenomenon. Under multipulse irradiation of the same area with relatively high overlapping of the irradiation spots as in the present experiments, accumulation of heat and defect states (the latter are abundant in yttria-stabilized zirconia [42]) can change the self-focusing conditions via creation of the thermal and defect convex lenses. Indeed, both terms $\Delta n_{th}$ and $\Delta n_{def}$ in Eq. (2) are positive [26,27,43] and can assist in the self-focusing effect. As for the two last terms in Eq. (2), $\Delta n_\rho$ and $\Delta n_P$, their roles in multipulse irradiation are more complicated. Heat accumulation in the delaminated layer should lead to a decrease of material density within the layer, ensuring $\Delta n_\rho < 0$. On the other hand, at each pulse within the light absorption region, material can be relocated with creation zones of higher and lower density as compared to the virgin one [34]. It could be speculated that a pressure-induced

compacted shell is created, which surrounds the pathway of the focused/self-focusing beam toward the focal region. This compacted shell, which is subjected also to the residual stress accumulation, should affect the propagation of the next laser pulse and, most plausibly, assist in guiding the light toward the plane of the beam collapse [44]. We note that the waveguiding effect of a transient lens created by a mutual action of thermal and defect-induced lenses, as well as by the material compaction shell, must also be inherent in direct laser writing of waveguides in optical glasses.

## IV. CONCLUSION

In this paper, we analyze ultrashort-pulse laser ablation of semitransparent materials in the example of YSZ ceramics. Unlike transparent (e.g., fused silica) or strongly absorbing (e.g., metals) materials, here the laser ablation process is strongly influenced by delamination of a relatively thick surface layer. The depth of the delamination (and hence the depth of the crater) depends on the interplay between Kerr self-focusing due to the positive nonlinear refractive index of the material and beam defocusing induced by free-electron plasma formation at the sample surface. As the free-electron plasma density is evolving during the laser pulse, the position where beam self-focusing may happen can also evolve in time. The actual position of the beam collapse is determined by the strength of a negative free-electon lens achieved during the pulse. When the incident pulse power increases, a denser free-electron shield is created on the sample surface that leads to a stronger antiwaveguiding effect and spatial delaying of the beam collapse. Our studies show that the unified ablation depth as a function of laser fluence [see Fig. 4(a)] can be better fitted by the linear dependence than by a logarithmic one, inherent in thermal mechanisms of ablation [45]. Together with the depth of observed delamination, which far exceeds the size of the laser irradiation spot, this result supports the relevance of the proposed phenomenological model. This modeling representation reasonably explains the dependence of the ablation depth on the laser fluence and provides an adequate quantitative estimation for the crater depth at the threshold of delamination.

At high laser fluences far exceeding the ablation threshold and strong overlaps between the irradiation spots upon processing, a paradoxical effect can be observed: no crater is left on the surface anymore, but instead the processed area rises up from the virgin sample surface; see, e.g., Fig. 7(a). It has been found that, in such cases, the delaminated layer is thick enough to withstand dynamic mechanical stresses and remains attached to the processed area as schematically shown in Fig. 9(e).

In summary, in this study, we demonstrate laser-induced delamination of layers with the thickness of several tens of micrometers and the area of nearly $5 \times 5$ mm$^2$ from the

bulk YSZ ceramics. It is shown that the delaminated layer thickness can be controlled by laser fluence and overlap of the irradiation spots upon laser scanning of samples. Consequently, the discovered effect opens up a method for controllable laser microslicing of brittle ceramic materials, i.e., cutting two-dimensional high-aspect-ratio sheets parallel to the bulk surface.

[1] M. Malinauskas, A. Žukauskas, S. Hasegawa, Y. Hayasaki, V. Mizeikis, R. Buividas, and S. Juodkazis, Ultrafast laser processing of materials: From science to industry, Light Sci. Appl. **5**, e16133 (2016).

[2] G. Paltauf and P. E. Dyer, Photomechanical processes and effects in ablation, Chem. Rev. **103**, 487 (2003).

[3] L. V. Zhigilei and B. J. Garrison, Mechanisms of laser ablation from molecular dynamics simulations: Dependence on the initial temperature and pulse duration, Appl. Phys. A **69**, S75 (1999).

[4] D. S. Ivanov and L. V. Zhigilei, Combined atomistic-continuum modeling of short-pulse laser melting and disintegration of metal films, Phys. Rev. B **68**, 064114 (2003).

[5] J. A. Fox and D. N. Barr, Laser-induced shock effects in plexiglas and 6061-T6 aluminum, Appl. Phys. Lett. **22**, 594 (1973).

[6] I. Gilath, D. Salzmann, M. Givon, M. Dariel, L. Kornblit, and T. Bar-Noy, Spallation as an effect of laser-induced shock waves, J. Mater. Sci. **23**, 1825 (1988).

[7] S. Eliezer, I. Gilath, and T. Bar-Noy, Laser-induced spall in metals: Experiment and simulation, J. Appl. Phys. **67**, 715 (1990).

[8] K. Sokolowski-Tinten, J. Bialkowski, A. Cavalleri, D. von der Linde, A. Oparin, J. Meyer-ter-Vehn, and S. I. Anisimov, Transient States of Matter During Short Pulse Laser Ablation, Phys. Rev. Lett. **81**, 224 (1998).

[9] H. Tamura, T. Kohama, K. Kondo, and M. Yoshida, Femtosecond-laser-induced spallation in aluminum, J. Appl. Phys. **89**, 3520 (2001).

[10] J. Koch, F. Korte, T. Bauer, C. Fallnich, A. Ostendorf, and B. N. Chichkov, Nanotexturing of gold films by femtosecond laser-induced melt dynamics, Appl. Phys. A **81**, 325 (2005).

[11] J.-M. Savolainen, M. S. Christensen, and P. Balling, Material swelling as the first step in the ablation of metals by ultrashort laser pulses, Phys. Rev. B, **84**(19), 193410 (2011).

[12] D. Puerto, J. Siegel, A. Ferrer, J. Hernandez-Rueda, and J. Solis, Correlation of the refractive index change at the surface and inside phosphate glass upon femtosecond laser irradiation, J. Opt. Soc. Am. B **29**, 2665 (2012).

[13] V. Zhakhovskii, N. Inogamov, and K. Nishihara, Laser ablation and spallation of crystalline aluminum simulated by molecular dynamics, J. Phys.: Conf. Ser. **112**, 042080 (2008).

[14] E. Kim, Y. Shimotsuma, M. Sakakura, and K. Miura, 4H-SiC wafer slicing by using femtosecond laser double-pulses, Opt. Mater. Express **7**, 2450 (2017).

[15] B. Butz, *Yttria-doped zirconia as solid electrolyte for fuel-cell applications: Fundamental aspects* (Suedwest-deutscher Verlag fuer Hochschulschriften, Saarbrücken, 2011).

[16] A. Selçuk and A. Atkinson, Elastic properties of ceramic oxides used in solid oxide fuel cells (SOFC), J. Eur. Ceram. Soc. **17**, 1523 (1997).

[17] T. Götsch, M. Stöger-Pollach, and S. Penner, in *European Microscopy Congress 2016: Proceedings* (Wiley-VCH Verlag GmbH & Co. KGaA, Weinheim, Germany, 2016), p. 724–725.

[18] R. Vaßen, Entwicklung neuer oxidischer Wärmedämm-schichten für Anwendungen in stationären und Flug-Gasturbinen: Zugl.: Bochum, Univ., Habil.-Schr., 2004, volume 33 of *Schriften des Forschungszentrums Jülich - Reihe Energietechnik* (Forschungszentrum, Jülich, 2004).

[19] R. Mendes Ribeiro, M. M. D. Ramos, A. M. Stoneham, and J. M. Correia Pires, Modelling of surface evaporation by laser ablation, Appl. Surf. Sci. **109–110**, 158 (1997).

[20] B. C. Stuart, M. D. Feit, S. Herman, A. M. Rubenchik, B. W. Shore, and M. D. Perry, Optical ablation by high-power short-pulse lasers, J. Opt. Soc. Am. B **13**, 459 (1996).

[21] G. A. Gogotsi, Y. L. Groushevsky, and K. K. Strelov, The significance of non-elastic deformation in the fracture of heterogeneous ceramic materials, Ceram. Int. **4**, 113 (1978).

[22] M. J. Weber, D. Milam, and W. L. Smith, Nonlinear refractive index of glasses and crystals, Opt. Eng. **17**, 463 (1978).

[23] S. V. Chekalin and V. P. Kandidov, From self-focusing light beams to femtosecond laser pulse lamentation, Phys. Usp. **56**, 123 (2013).

[24] J. H. Marburger, Self-focusing: Theory, Prog. Quant. Electr. **4**, 35 (1975).

[25] A. Couairon and A. Myzyrowicz, Femtosecond filamentation in transparent media, Phys. Rep. **441**, 47 (2007).

[26] R. M. Waxler and G. W. Cleek, The effect of temperature and pressure on the refractive index of some oxide glasses, J. Res. Nat. Bur. Stand. Sec. A: Phys. Ch. **77**, 755 (1973).

[27] M. Sakakura, M. Terazima, Y. Shimotsuma, K. Miura, and K. Hirao, Thermal and shock induced modification inside a silica glass by focused femtosecond laser pulse, J. Appl. Phys. **109**, 023503 (2011).

[28] N. M. Bulgakova, V. P. Zhukov, and Y. P. Meshcheryakov, Theoretical treatments of ultrashort pulse laser processing of transparent materials: Toward understanding the volume nanograting formation and "quill" writing effect, Appl. Phys. B **113**, 437 (2013).

[29] I. M. Burakov, N. M. Bulgakova, R. Stoian, A. Rosenfeld, and I. V. Hertel, Theoretical investigations of material modification using temporally shaped femtosecond laser pulses, Appl. Phys. A **81**, 1639 (2005).

[30] M. Lenzner, F. Krausz, J. Krüger, and W. Kautek, Photoablation with sub-10 fs laser pulses, Appl. Surf. Sci. **154–155**, 11 (2000).

[31] B. Rethfeld, D. S. Ivanov, M. E. Garcia, and S. I. Anisimov, Modelling ultrafast laser ablation, J. Phys. D: Appl. Phys. **50**, 193001 (2017).

[32] S. Ostanin, A. J. Craven, D. W. McComb, D. Vlachos, A. Alavi, M. W. Finnis, and A. T. Paxton, Effect of relaxation on the oxygen k-edge electron energy-loss near-edge structure in yttria-stabilized zirconia, J. Opt. Soc. Am. B **62**, 14728 (2005).

[33] M. Mero, J. Liu, W. Rudolph, D. Ristau, and K. Starke, Scaling laws of femtosecond laser pulse induced breakdown in oxide films, Phys. Rev. B **71**, 115109 (2005).

[34] N. M. Bulgakova, V. P. Zhukov, S. V. Sonina, and Y. P. Meshcheryakov, Modification of transparent materials with ultrashort laser pulses: What is energetically and mechanically meaningful? J. Appl. Phys. **118**, 233108 (2015).

[35] I. Mirza, N. M. Bulgakova, J. Tomáštík, V. Michálek, O. Haderka, L. Fekete, and T. Mocek, Ultrashort pulse laser ablation of dielectrics: Thresholds, mechanisms, role of breakdown, Sci. Rep. **6**, 39133 (2016).

[36] G. Geoffroy, G. Duchateau, N. Fedorov, P. Martin, and S. Guizard, Influence of electron coulomb explosion on photoelectron spectra of dielectrics irradiated by femtosecond laser pulses, Las. Phys. **24**, 086101 (2014).

[37] J. W. Adams, R. Ruh, and K. S. Mazdiyasni, Young's modulus, flexural strength, and fracture of yttria-stabilized zirconia versus temperature, J. Am. Ceram. Soc. **80**, 903 (1997).

[38] H. Hayashi, T. Saitou, N. Maruyama, H. Inaba, K. Kawamura, and M. Mori, Thermal expansion coefficient of yttria stabilized zirconia for various yttria contents, Solid State Ionics **176**, 613 (2005).

[39] W. D. Kingery, Factors affecting thermal stress resistance of ceramic materials, J. Am. Ceram. Soc. **38**, 3 (1955).

[40] K. Noguchi, M. Fujita, T. Masaki, and M. Mizushina, Tensile strength of yttria-stabilized tetragonal zirconia polycrystals, J. Am. Ceram. Soc. **72**, 305 (1997).

[41] A. Rosenfeld, M. Lorenz, R. Stoian, and D. Ashkenasi, Ultrashort-laser-pulse damage threshold of transparent materials and the role of incubation, Appl. Phys. A **69**, S373 (1999).

[42] A. S. Foster, V. B. Sulimov, F. Lopez Gejo, A. L. Shluger, and R. M. Nieminen, Modelling of point defects in monoclinic zirconia, J. Non Cryst. Solids **303**, 101 (2002).

[43] P. Martin, S. Guizard, G. Petite, P. D'Oliveira, P. Meynadier, and M. Perdrix, Subpicosecond study of carrier trapping dynamics in wide-band-gap crystals, Phys. Rev. B **55**, 5799 (1997).

[44] J. W. Chan, T. R. Huser, S. H. Risbud, J. S. Hayden, and D. M. Krol, Waveguide fabrication in phosphate glasses using femtosecond laser pulses, Appl. Phys. Lett. **82**, 2371 (2003).

[45] B. N. Chichkov, C. Momma, S. Nolte, F. von Alvensleben, and A. Tünnermann, Femtosecond, picosecond and nanosecond laser ablation of solids, Appl. Phys. A **63**, 109 (1996).